journal homepage: www.brodogradnja.fsb.hr

Brodogradnja

An International Journal of Naval Architecture and Ocean Engineering for Research and Development

An optimized method for AUV trajectory model in benthonic hydrothermal area based on improved slime mold algorithm

Chunmeng Jiang[1], Yiming Tang[1], Jianguo Wang[2], Wenchao Zhang[1], Min Zhou[1], Jiaying Niu[1], Lei Wan[3], Guofang Chen[3], Gongxing Wu[4], Xide Cheng[5]*

Affiliation
[1] *Wuhan Institute of Shipbuilding Technology, Wuhan 430050, China*
[2] *China Ship Development and Design Center, Wuhan 430064, China;*
[3] *School of Naval Engineering, Harbin Engineering University, Harbin 150001, China;*
[4] *College of Ocean Science and Engineering, Shanghai Maritime University, Shanghai 201306, China;*
[5] *School of Naval Architecture, Ocean and Energy Power Engineering, Wuhan University of Technology, Wuhan 430063, China*

ARTICLE INFO

Editor-in-Chief: Prof. Nastia Degiuli
Associate Editor: PhD Ivana Martić

Autonomous underwater vehicle
Benthonic hydrothermal area
Trajectory tracking model
Improved slime mold algorithm

ABSTRACT

The optimization of the desired autonomous underwater vehicle (AUV) trajectory modeling and AUV trajectory tracking control in the benthonic hydrothermal area were studied. In the conventional trajectory tracking model construction methods, the time points were roughly combined with the position points of the planned path, making it difficult to produce a smooth trajectory. Although the spline interpolation method was an ideal option for smooth curves, a great number of points were needed for a complex desired trajectory mode. In response to the demanding requirements of AUV trajectory tracking control in the benthonic hydrothermal area, an under-actuated test platform was first established, and the cubic spline interpolation was adopted to process the preset path points for a smooth desired trajectory. An improved slime mold algorithm (SMA) was put forward to optimize the interpolating points used in the trajectory modeling. The Levy flight technology and the compactness technique to speed up the search process and increase the search accuracy. The simulation experiments were conducted in comparison with the artificial fish swarm algorithm (AFSA), the particle swarm optimization (PSO), and the compact cuckoo search (CCS). The results showed that the improved SMA shortened the search process, effectively avoided the local extreme values, and generated a high-precision desired trajectory model in a shorter time. The pool test also verified the feasibility and effectiveness of the proposed method. The method proposed in this study can satisfy the modeling of benthonic hydrothermal trajectory with a fewer number of nodes, faster search progress and search accuracy.

1. Introduction

As the offshore and shallow offshore waters have been fully explored and exploited, the deep sea is becoming one of the hottest spots of marine development [1]. The deep sea is known for new resources such

* Corresponding author.
E-mail address: 0004146@mail.wspc.edu.cn

http://dx.doi.org/10.21278/brod75401
Submitted 11.04.2024.; Accepted 10.07.2024.
ISSN 0007-215X; eISSN 1845-5859

as polymetallic nodules, hydrothermal sulfides, and natural gas hydrates, especially the benthonic hydrothermal activities and extreme ecosystems that are of significant value to scientific research and commercial application. The rapid advancement in artificial intelligence, computer simulation, machine learning, intelligent optimization, and intelligent control technologies [2-10] has also brought breakthroughs to underwater vehicle technologies. With small size, light weight, high flexibility, autonomy and efficiency, autonomous underwater vehicles (AUVs) are playing an increasingly important role in the complex contexts to which divers have difficult access, including exploration of the deep-sea hydrothermal areas, development of deep-sea mineral resources, utilization of deep-sea gas hydrates, detection of near-bottom shipwreck, cable maintenance, pipeline, and optical fiber laying [11-17], etc. Regarding the dispersed flows, active hydrothermal vents and challenging environment at the benthonic hydrothermal areas, together with the potentially saturated AUV actuators and propeller failure, near-bottom detection operations require robust and stable trajectory tracking control effects to which the desired trajectory model is a key part.

Azeez Muhammad I et al [18] studied PID-based modeling and trajectory tracking control of underwater vehicles using the Lyapunov function. The application of particle swarm optimization, artificial bee colony algorithm, artificial fish swarm algorithm and marine predator algorithm was compared. The superiority of the proposed method was proved by simulation experiments. Wang et al [19] designed a robust trajectory tracking control method for AUVs with a hybrid propulsion system. A double-loop trajectory tracking control structure was proposed considering model uncertainties and external interference. The comparative simulation experiments verified the feasibility of the proposed method. A dynamic modeling and trajectory tracking method for underwater vehicles [20] was studied and a comparison was made with the sliding mode controller, PID controller and fuzzy logic controller. The effectiveness of the proposed method was verified by different trajectories. Chen et al [21] focused on AUV trajectory tracking control with a high-order adaptive observer. A continuous timing sliding mode surface was designed to improve the convergence performance, together with an adaptive fault-tolerant tracking control law. The effectiveness and superiority of the proposed method were verified in simulation experiments. Wu et al [22] proposed a novel method based on an active interference compensation mechanism to improve control performance. An extended sliding mode observer and a linear extended state observer were designed. The stability analysis and simulation experiments verified the advantages of the proposed method. Bao et al [23] combined the genetic algorithm of normal population probability distribution with ant colony optimization in trajectory model predictive control. The robustness of the aforesaid combination was verified by simulation experiments. A fast trajectory tracking control method was proposed by Dong et al [24]. A trajectory tracking control system was established with auxiliary variables and bi-variables introduced. Xiao et al [25] came up with a method of model predictive trajectory tracking control of unmanned vehicles based on radial basis function neural network optimization. Two optimal model predictive control trajectory tracking control systems were designed based on adaptive compensation and robust control. Focusing on multiple under-actuated AUV formation control, Qian et al [26] proposed a new consensus-based model predictive control with optimized line-of-sight guidance. The effectiveness and robustness of the proposed controller were verified by Lyapunov stability analysis and numerical simulations. Yu et al [27] designed a nonlinear model predictive controller using a genetic algorithm for ship trajectory tracking. Real-time parameters optimization was achieved through the genetic algorithm, which improved the efficiency and accuracy of the controller. Contrastive experiments with different weights were carried out to prove better local control accuracy of the proposed method. Duan et al [28] proposed a reinforcement learning-based model-free AUV trajectory tracking strategy. Wang et al [29] studied a robust adaptive three-dimensional trajectory tracking method for unmanned underwater vehicles. A double closed-loop controller containing nonlinear model predictive control and adaptive sliding-mode control was designed. Simulation experiments verified the effectiveness of the proposed controller. Wang et al [30] concentrated on AUV trajectory tracking control based on the time-delay adaptive high-order sliding mode method considering the deficiency in sensing precision and external disturbance. Zhu et al [31] proposed a trajectory tracking controller based on finite-time sliding mode control and radial-basis function neural network observer. A single-parameter online weight-updating technique was adopted. Passive fault diagnosis was used to deal with actuator failure and input saturation. The feasibility of the proposed controller was verified in simulation experiments. A high-order sliding mode model-free controller was proposed for the 6-DOF trajectory tracking

control [32]. The Kalman filter was adopted in the estimation of measurement error to correct the positioning system. The contrastive simulation experiments with the PID controller showed the superiority of the proposed method. Thanh Pham Nguyen Nhut et al [33] focused on adaptive fuzzy 3D trajectory tracking control. An adaptive fuzzy dynamic surface controller was used to eliminate system constraints. The stability analysis and the numerical simulations proved the feasibility and effectiveness of the proposed method. Herman Przemyslaw [34] studied the trajectory tracking nonlinear control of under-actuated AUV by velocity transformation considering the external disturbance. The theoretical results were followed up with simulation tests conducted on a model with three degrees of freedom for two underwater vehicles. Bingul Zafer et al [35] designed a hybrid controller for model-free AUV trajectory tracking control. The intelligent PID and PD feedforward controller were combined to counter disturbance and compensate for the initial tracking errors. Numerical simulation experiments were carried out under different disturbing conditions, the results of which showed desirable trajectory tracking performance and resistance to external disturbance. Sedghi Fatemeh et al [36] proposed a filter-based neural adaptive robust finite-time trajectory tracking strategy. The artificial neural network and finite-time adaptive control law were adopted to approximate the nonlinear characteristics of the AUV. A new generalized superspiral controller was designed [37] for AUV trajectory tracking control, with a finite-time estimator introduced to predict the hydrodynamic characteristics of the AUV. Simulation experiments verified the effectiveness of the proposed controller. Ma et al [38] considered the external disturbance and input saturation in AUV trajectory tracking control. An extended state observer and a saturation controller were designed to deal with the disturbance. The experimental results verified the superiority of the proposed observer and controller. Xue et al [39] concentrated on AUV-manipulator trajectory tracking control. A model-free adaptive control method combined with a radial basis function neural network was designed to improve the controller performance. The above trajectory tracking control methods have generally satisfied the requirement of control accuracy and a few have been adopted in engineering practice, but research on trajectory tracking modeling and optimization in benthonic hydrothermal areas is scarce. In present trajectory tracking control studies, the desired tracking model is typically established with casually combined time points and position points, which makes it difficult to ensure a smooth trajectory. Although the cubic splines can be used to smooth curve fitting, a large number of nodes are required in the cubic spline interpolation method in the case of complex curves in high-precision models. The great number of nodes will lead to piecewise functions that result in demanding calculation and abrupt control outputs.

In response to the demanding workload and deficiency of the present studies, an improved slime mold algorithm (iSMA) is developed to optimize the interpolating points used in the trajectory model construction process, with the Levy flight technology to improve the global search ability and the compactness technique to increase the search accuracy. The trajectory modeled on the proposed algorithm can ensure sufficient exploration of the target area with coverage of key locations which is especially applicable to benthonic hydrothermal area.

The research is organized as follows. The first section provides information on the test platform, including the structure design, software and hardware systems of the platform. The second section focuses on the modeling and analysis of AUV movement in the hydrothermal environment. The third section explains the optimization method for the desired AUV trajectory model based on the slime mold algorithm, including the cubic spline interpolation, the basic slime mold algorithm, and its improved version with the Levy flight technology and compactness technique. The fourth and fifth sections provide the results of simulation experiments and field trials to prove the feasibility and effectiveness of the proposed optimization method for AUV trajectory modeling in hydrothermal area operations.

2. Test platform

The test platform is designed as shown in Figure 1. The modular structure allows situational loads and equipment according to task requirements. The AUV is composed of a light shell and a pressure shell. The streamlined light shell reduces resistance in control movement [40]. The segmented pressure shell contains three watertight compartments for control, sensing and propulsion. The control compartment and the sensing compartment are connected by a uniform cylindrical structure where devices and ballast irons are carried. The

sensing compartment and the propulsion compartment are connected and fixed by flanges with buoyancy materials. The propulsion compartment at the tail is packaged with two pairs of steering engines (vertical and horizontal) and a propeller. The rudder-propeller configuration at the tail enables the AUV to move in the heading, pitching dimensions and surge, heave directions [41].

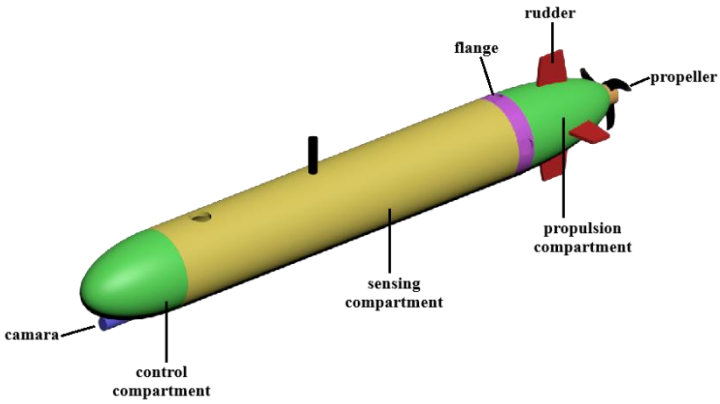

Fig. 1 Profile of the test platform

The test platform integrates the intelligent planning system, the navigation system, the motion control system, the sensing system, the emergency system, etc. [42]. The platform functions based on the PC104 bus, the CPU board, the power board, the DIO board, and the AD board [43]. The hardware architecture is shown in Figure 2. The PC/104 bus realizes the communication between systems. The emergency system enables the platform to come up to the surface when it reaches the depth limit. The intelligent planning system calculates and delivers the target instructions. The navigation system provides accurate position information. The motion control system acquires and decodes sensor data, runs the control algorithms, and transmits thrust commands to the propeller and angle commands to the rudders. The sensing system collects data on depth, heading angle, trimming angle, heeling angle, velocity, and water leakage based on the sensors equipped. The VxWorks real-time system ensures reliable and timely operations during underwater movement [44]. VxWorks completed the initialization of each system, provided the communication channels with the corresponding devices, and determined the circulation frequency of the main function [45-46]. The software architecture is shown in Figure 3. The information workflow is as follows. According to the control target, the planning and calculating unit delivers the target instructions to the control command unit. After initialization of the control mode and the control parameters, the control command unit sends the control target to the thrust distribution unit according to the calculation results based on the sensor data. Finally, the outputs of the thrust distribution unit drive the platform toward the target via the propeller and the rudders.

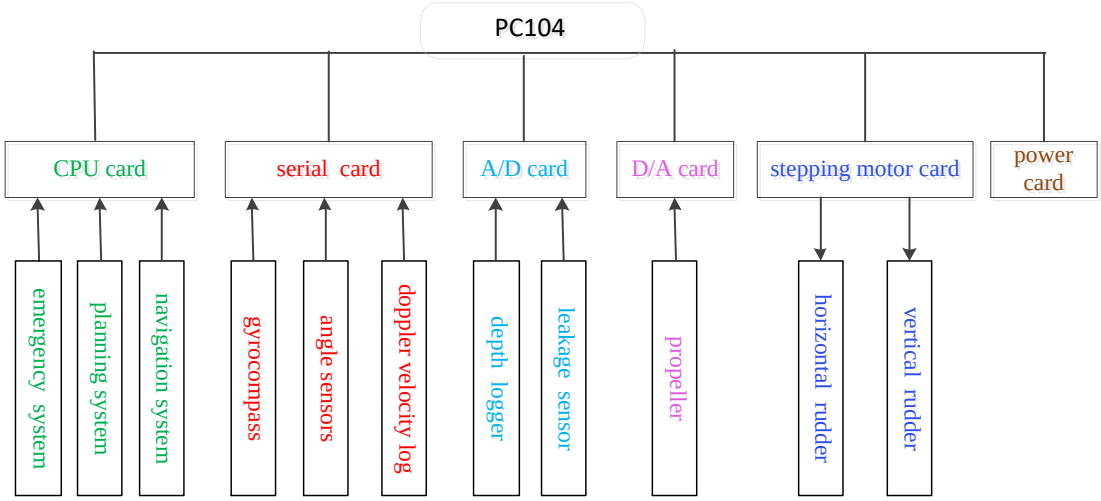

Fig. 2 Hardware architecture of the platform

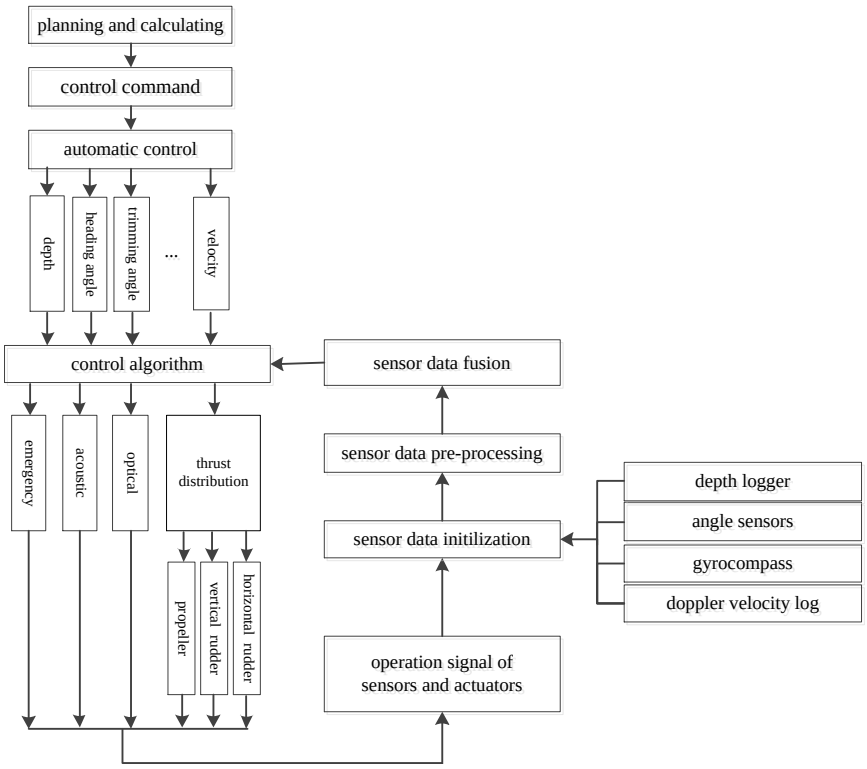

Fig. 3 Software architecture of the platform

3. Modeling and analysis of AUV movement in hydrothermal context

3.1 Modeling of AUV movement system

The under-actuated AUV is assumed three symmetrical planes according to its exterior. The movement model in six degrees of freedom (DOFs) can be simplified as follows:

$$\begin{aligned} &\dot{\eta} = J(\eta)\upsilon \\ &M\dot{\upsilon} = -C_A(\upsilon)\upsilon - D(\upsilon)\upsilon - C_{RB}(\upsilon)\upsilon - g(\eta) + \tau_\upsilon \end{aligned} \tag{1}$$

where η is the vector of position and attitude angle in the geodetic coordinate system, J the transformation matrix between the body coordinate system and the geodetic coordinate system, υ the vector of linear velocity and angular velocity [47], M the inertia matrix, $C_A(\upsilon)$ the Coriolis force matrix, $D(\upsilon)$ the damping matrix of the AUV, $C_{RB}(\upsilon)$ the centripetal force matrix of the rigid body, $g(\eta)$ the righting force and moment caused by gravity and buoyancy and τ_υ the control output.

$$\dot{\eta} = J(\eta)\upsilon \Leftrightarrow \begin{bmatrix} \dot{\eta}_1 \\ \dot{\eta}_2 \end{bmatrix} = \begin{bmatrix} J_1(\eta_2) & 0_{3\times3} \\ 0_{3\times3} & J_2(\eta_2) \end{bmatrix} \begin{bmatrix} \upsilon_1 \\ \upsilon_2 \end{bmatrix} \tag{2}$$

where $J_1(\eta)$ is the transformation matrix between variables of linear velocity and position, $J_2(\eta)$ the transformation matrix between variables of angular velocity and attitude angle:

$$J_1(\eta_2) = \begin{bmatrix} \mathrm{c}(\theta)\mathrm{c}(\psi) & \mathrm{s}(\phi)\mathrm{s}(\theta)\mathrm{c}(\psi) - \mathrm{c}(\phi)\mathrm{s}(\psi) & \mathrm{s}(\phi)\mathrm{s}(\psi) + \mathrm{c}(\phi)\mathrm{s}(\theta)\mathrm{c}(\psi) \\ \mathrm{c}(\theta)\mathrm{c}(\psi) & \mathrm{s}(\phi)\mathrm{s}(\theta)\mathrm{s}(\psi) + \mathrm{c}(\phi)\mathrm{c}(\psi) & \mathrm{s}(\phi)\mathrm{s}(\theta)\mathrm{s}(\psi) - \mathrm{s}(\phi)\mathrm{c}(\psi) \\ -\mathrm{s}(\theta) & \mathrm{s}(\phi)\mathrm{c}(\theta) & \mathrm{c}(\phi)\mathrm{c}(\theta) \end{bmatrix} \tag{3}$$

$$J_2(\eta_2)=\begin{bmatrix}1 & t(\theta)s(\psi) & t(\theta)c(\psi)\\ 0 & c(\psi) & s(\psi)\\ 0 & s(\psi)/c(\theta) & c(\psi)/c(\theta)\end{bmatrix} \tag{4}$$

where ϕ stands for the rolling angle, θ for the trimming angle, ψ for the heading angle, s( ) for sine, c( ) for cosine and t( ) for the tangent.

$$M=\begin{bmatrix}m-X_{\dot{u}} & 0 & 0 & 0 & 0 & 0\\ 0 & m-Y_{\dot{v}} & 0 & 0 & 0 & 0\\ 0 & 0 & m-Z_{\dot{w}} & 0 & 0 & 0\\ 0 & 0 & 0 & I_x-K_{\dot{p}} & 0 & 0\\ 0 & 0 & 0 & 0 & I_y-M_{\dot{q}} & 0\\ 0 & 0 & 0 & 0 & 0 & I_z-N_{\dot{r}}\end{bmatrix} \tag{5}$$

where m is the mass of the AUV. I_x, I_y and I_z are the inertia moments. $X_{\dot{u}}$, $Y_{\dot{u}}$, $Z_{\dot{w}}$, $N_{\dot{r}}$ are the first-order hydrodynamic coefficients.

$$C_A(\upsilon)=\begin{bmatrix}0 & 0 & 0 & 0 & -a_3 & a_2\\ 0 & 0 & 0 & a_3 & 0 & -a_1\\ 0 & 0 & 0 & -a_2 & a_1 & 0\\ 0 & -a_3 & a_2 & 0 & -b_3 & b_2\\ a_3 & 0 & -a_1 & b_3 & 0 & -b_1\\ -a_2 & a_1 & 0 & -b_2 & b_1 & 0\end{bmatrix} \tag{6}$$

$$\begin{aligned}
a_1 &= X_{\dot{u}}u+X_{\dot{v}}v+X_{\dot{w}}w+X_{\dot{p}}p+X_{\dot{q}}q+X_{\dot{r}}r\\
a_2 &= Y_{\dot{u}}u+Y_{\dot{v}}v+Y_{\dot{w}}w+Y_{\dot{p}}p+Y_{\dot{q}}q+Y_{\dot{r}}r\\
a_3 &= Z_{\dot{u}}u+Z_{\dot{v}}v+Z_{\dot{w}}w+Z_{\dot{p}}p+Z_{\dot{q}}q+Z_{\dot{r}}r\\
b_1 &= K_{\dot{u}}u+K_{\dot{v}}v+K_{\dot{w}}w+K_{\dot{p}}p+K_{\dot{q}}q+K_{\dot{r}}r\\
b_2 &= M_{\dot{u}}u+M_{\dot{v}}v+M_{\dot{w}}w+M_{\dot{p}}p+M_{\dot{q}}q+M_{\dot{r}}r\\
b_3 &= N_{\dot{u}}u+N_{\dot{v}}v+N_{\dot{w}}w+N_{\dot{p}}p+N_{\dot{q}}q+N_{\dot{r}}r
\end{aligned} \tag{7}$$

$$D(\upsilon)=D+D_n(\upsilon) \tag{8}$$

where $D(\upsilon)$ means the damping matrix, D the linear damping matrix and $D_n(\upsilon)$ the nonlinear damping matrix:

$$D=-\begin{bmatrix} X_u & X_v & X_w & X_p & X_q & X_r \\ Y_u & Y_v & Y_w & Y_p & Y_q & Y_r \\ Z_u & Z_v & Z_w & Z_p & Z_q & Z_r \\ K_u & K_v & K_w & K_p & K_q & K_r \\ M_u & M_v & M_w & M_p & M_q & M_r \\ N_u & N_v & N_w & N_p & N_q & N_r \end{bmatrix} \tag{9}$$

$$D_n(\upsilon)=-\mathrm{diag}\left(X_{u|u|}|u|, Y_{v|v|}|v|, Z_{w|w|}|w|,\ K_{p|p|}|p|, M_{q|q|}|q|, N_{r|r|}|r|\right) \tag{10}$$

$$C_{RB}(\upsilon)=\begin{bmatrix} 0 & 0 & 0 \\ 0 & 0 & 0 \\ 0 & 0 & 0 \\ -m(y_G q+z_G r) & m(y_G p+w) & m(z_G p-v) \\ m(x_G q-w) & -m(z_G+x_G p) & -m(z_G p+u) \\ m(x_G r+v) & -m(y_G r-u) & -m(x_G p+y_G p) \end{bmatrix} \begin{bmatrix} m(y_G q+z_G r) & -m(x_G p-w) & -m(x_G r+v) \\ -m(y_G p+w) & m(z_G+x_G p) & -m(y_G-u) \\ m(z_G p-v) & -m(z_G p+u) & m(x_G p+y_G p) \\ 0 & -I_{yz}q-I_{xz}p+I_z r & I_{yz}r+I_{xy}p-I_y q \\ I_{yz}q+I_{xz}p-I_z r & 0 & -I_{xz}r-I_{xy}q+I_x p \\ -I_{yz}r-I_{xy}p+I_y q & I_{xz}r+I_{xy}q-I_x p & 0 \end{bmatrix} \tag{11}$$

$$g(\eta)=\begin{bmatrix} (W-B)\mathrm{s}(\theta) \\ -(W-B)\mathrm{c}(\theta)\mathrm{s}(\phi) \\ -(W-B)\mathrm{c}(\theta)\mathrm{c}(\phi) \\ -(y_G W-y_B B)\mathrm{c}(\theta)\mathrm{c}(\phi)+(z_G W-z_B B)\mathrm{c}(\theta)\mathrm{s}(\phi) \\ (z_G W-z_B B)\mathrm{s}(\theta)+(x_G W-x_B B)\mathrm{c}(\theta)\mathrm{c}(\phi) \\ -(x_G W-x_B B)\mathrm{c}(\theta)\mathrm{s}(\phi)-(y_G W-y_B B)\mathrm{s}(\theta) \end{bmatrix} \tag{12}$$

where W and B are respectively the gravity and the buoyancy of the AUV. (x_G, y_G, z_G) and (x_B, y_B, z_B) stand for respectively the positions of the gravity center and the buoyancy center of the AUV.

The movement model in Equation (1) is featured with the following properties:

Property I. M is a positive definite matrix. $M=M^T>0$

Property II. $C_A(\upsilon)=-C_A{}^T(\upsilon), \forall \upsilon \in \Re^6$

Property III. In accordance with the layout and configuration of the actuators, the control input τ_υ satisfies $\tau_\upsilon=\left[\tau_X, 0, \tau_Z, \tau_K, \tau_M, \tau_N\right]^T$. The movement in three DOFs (surge, sway and yaw) needs two control inputs (thrusting force in the surge direction and moment in the yaw dimension).

Property IV. Due to the absence of lateral thrusters, the thrusting force in the surge direction and the moment in the yaw dimension are organized and combined to achieve precise tracking in the sway direction at the same time as tracking in the surge direction and yaw dimension.

With the parameter matrices in the three DOFs on the horizontal plane, the AUV movement model can be expressed as follows:

$$\begin{cases} \dot{x} = uc(\psi) - vs(\psi) \\ \dot{y} = us(\psi) + vc(\psi) \\ \dot{\psi} = r \end{cases}$$

$$\begin{cases} \left(m - X_{\dot{u}}\right)\dot{u} + \left(a_2\left(u_r, v_r, w_r\right) - mv\right)r - \left(X_u + X_{u|u|}\left|u_r\right|\right)u_r + (W - B)s(q) = t_X \\ \left(m - Y_{\dot{v}}\right)\dot{v} + \left(mu - a_1\left(u_r, v_r, w_r\right)\right)r - \left(Y_v + Y_{v|v|}\left|v_r\right|\right)v_r - (W - B)c(q)s(j) = 0 \\ \left(I_z - N_{\dot{r}}\right)\dot{r} + \left(a_1\left(u_r, v_r, w_r\right)v_r - a_2\left(u_r, v_r, w_r\right)u_r\right) - \left(N_r + N_{r|r|}\left|r\right|\right)r \\ \qquad\qquad - (x_G W - x_B B)c(q)s(j) - (y_G W - y_B B)s(q) = t_N \end{cases} \tag{13}$$

3.2 Analysis of benthonic hydrothermal environment

The benthonic hydrothermal areas are featured with challenging and complex conditions [48] with plentiful hydrothermal deposits as shown in Figure 4. The stratiform terrain forms in areas of abundant magma supply and separate faults form where the magma supply is insufficient. Moreover, the hydrothermal fluids ejecting from the craters shown in Figure 5 at a high initial velocity are jammed within a narrow channel, which will influence the trajectory tracking operations in pinnate waters. In addition, changes in temperature and chemical compositions of local seawater caused by the active hydrothermal deposits are also great challenges to AUV trajectory tracking control [49-50].

Fig.4 Deposits in hydrothermal area

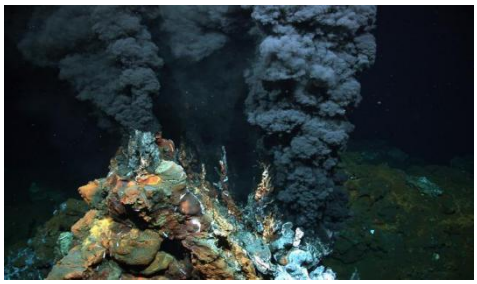

Fig.5 Hydrothermal vents

4. Optimization of desired trajectory model with improved slime mold algorithm

4.1 Trajectory model with cubic spline interpolation

The model of the hydrothermal terrain to be explored is established as shown in Figure 6. According to the exploration task, the AUV is expected to descend along the gentle slope and then travel at a fixed height of 2m near the bottom throughout the dense deposit area and finally circle the active hydrothermal vent.

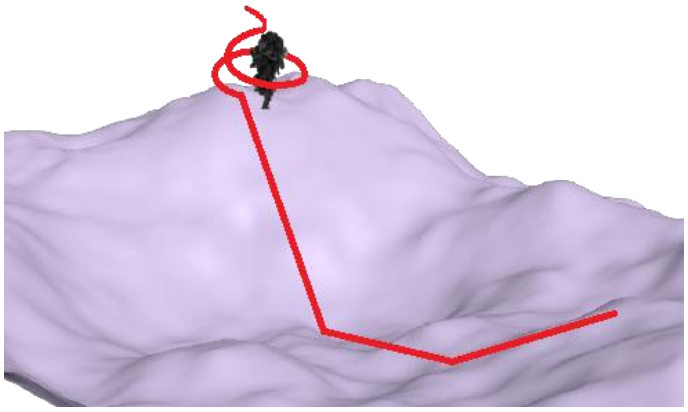

Fig.6 AUV detection route near the bottom

The desired trajectory model describes the three-dimensional spatial route from the starting point P1 to the hydrothermal vent P2 within the time interval $[T_1, T_n]$. n path points are selected. The selected points of position and time are simplified as follows:

$$P_j = \left(X_j, Y_j, Z_j\right) @ T_j \tag{14}$$

where T_j is the time point when the AUV is expected to reach the position point P_j, $j = 1,2,\ldots,n$. The cubic spline interpolation [51] is adopted to mathematically connect the position states X_j, Y_j, Z_j with time point T_j, with the boundary conditions satisfied at $\left(X_1, Y_1, Z_1\right)$ and $\left(X_n, Y_n, Z_n\right)$.

The position state variables in the desired trajectory can be expressed as follows:

$$\begin{aligned} x_{1d} &= \text{spline}\left(X, T_a, t_1\right) \\ y_{1d} &= \text{spline}\left(Y, T_a, t_1\right) \\ z_{1d} &= \text{spline}\left(Z, T_a, t_1\right) \end{aligned} \tag{15}$$

where $X = \left[X_1 \ldots X_n\right] \in R^{1\times n}$, $Y = \left[Y_1 \ldots Y_n\right] \in R^{1\times n}$, $Z = \left[Z_1 \ldots Z_n\right] \in R^{1\times n}$ are the selected desired position points. $T_a = \left[T_1 \ldots T_n\right] \in R^{1\times n}$ is the time interval and t_1 is the desired total time to complete the trajectory. According to the cubic spline interpolation method, the entire desired trajectory is constructed by (n-1) functions with each function expressed as follows:

$$\begin{cases} x_{1d}(i,1) = x_{1d}.\text{coefs}(i,1)\left(t - x_{1d}.\text{breaks}(i)\right)^3 + x_{1d}.\text{coefs}(i,2)\left(t - x_{1d}.\text{breaks}(i)\right)^2 \\ \qquad + x_{1d}.\text{coefs}(i,3)\left(t - x_{1d}.\text{breaks}(i)\right) + x_{1d}.\text{coefs}(i,4) \\ y_{1d}(i,1) = y_{1d}.\text{coefs}(i,1)\left(t - y_{1d}.\text{breaks}(i)\right)^3 + y_{1d}.\text{coefs}(i,2)\left(t - y_{1d}.\text{breaks}(i)\right)^2 \\ \qquad + y_{1d}.\text{coefs}(i,3)\left(t - y_{1d}.\text{breaks}(i)\right) + y_{1d}.\text{coefs}(i,4) \\ z_{1d}(i,1) = z_{1d}.\text{coefs}(i,1)\left(t - z_{1d}.\text{breaks}(i)\right)^3 + z_{1d}.\text{coefs}(i,2)\left(t - z_{1d}.\text{breaks}(i)\right)^2 \\ \qquad + z_{1d}.\text{coefs}(i,3)\left(t - z_{1d}.\text{breaks}(i)\right) + z_{1d}.\text{coefs}(i,4) \end{cases} \quad T_i \le t \le T_{i+1} \tag{16}$$

where $x_{1d}.\text{coefs} \in R^{(n-1)\times 4}$, $y_{1d}.\text{coefs} \in R^{(n-1)\times 4}$, $z_{1d}.\text{coefs} \in R^{(n-1)\times 4}$ are the function coefficients obtained by cubic spline interpolation. $x_{1d}.\text{breaks} \in R^{1\times(n-1)}$, $y_{1d}.\text{breaks} \in R^{1\times(n-1)}$, $z_{1d}.\text{breaks} \in R^{1\times(n-1)}$ are the break points.

$\phi_d = 0$ rad and $\theta_d = 0$ rad are constant attitude angles in the desired trajectory model. Based on the position trajectory results in Equations (15) and (16), the mathematical model of heading angle is established as follows:

$$\psi_{1d} = spline\left(Yaw, T_a, t_1\right)$$

$$\begin{aligned}\psi_{1d}(i,1) = {} & \psi_{1d}.\text{coefs}(i,1)\left(t - \psi_{1d}.\text{breaks}(i)\right)^3 + \psi_{1d}.\text{coefs}(i,2)\left(t - \psi_{1d}.\text{breaks}(i)\right)^2 \\ & + \psi_{1d}.\text{coefs}(i,3)\left(t - \psi_{1d}.\text{breaks}(i)\right) + \psi_{1d}.\text{coefs}(i,4) \qquad T_i \le t \le T_{i+1}\end{aligned} \tag{17}$$

where $Yaw = \left[Yaw_1 \ldots Yaw_n\right] \in R^{1\times n}$ is the heading angle set of the selected path points. $\psi_{1d}.\text{coefs} \in R^{(n-1)\times 4}$ and $\psi_{1d}.\text{breaks} \in R^{1\times(n-1)}$ are respectively the function coefficients and corresponding breakpoints of the desired heading angles calculated by cubic spline interpolation.

With Equations (16) and (17), the desired trajectory model for the target hydrothermal area is established as follows.

$$\begin{cases} x_{1d}(i,1) = x_{1d}.\text{coefs}(i,1)\left(t - x_{1d}.\text{breaks}(i)\right)^3 + x_{1d}.\text{coefs}(i,2)\left(t - x_{1d}.\text{breaks}(i)\right)^2 \\ \quad + x_{1d}.\text{coefs}(i,3)\left(t - x_{1d}.\text{breaks}(i)\right) + x_{1d}.\text{coefs}(i,4) \\ y_{1d}(i,1) = y_{1d}.\text{coefs}(i,1)\left(t - y_{1d}.\text{breaks}(i)\right)^3 + y_{1d}.\text{coefs}(i,2)\left(t - y_{1d}.\text{breaks}(i)\right)^2 \\ \quad + y_{1d}.\text{coefs}(i,3)\left(t - y_{1d}.\text{breaks}(i)\right) + y_{1d}.\text{coefs}(i,4) \\ z_{1d}(i,1) = z_{1d}.\text{coefs}(i,1)\left(t - z_{1d}.\text{breaks}(i)\right)^3 + z_{1d}.\text{coefs}(i,2)\left(t - z_{1d}.\text{breaks}(i)\right)^2 \qquad T_i \le t \le T_{i+1} \\ \quad + z_{1d}.\text{coefs}(i,3)\left(t - z_{1d}.\text{breaks}(i)\right) + z_{1d}.\text{coefs}(i,4) \\ \phi_{1d}(i,1) = 0 \\ \theta_{1d}(i,1) = 0 \\ \psi_{1d}(i,1) = \psi_{1d}.\text{coefs}(i,1)\left(t - \psi_{1d}.\text{breaks}(i)\right)^3 + \psi_{1d}.\text{coefs}(i,2)\left(t - \psi_{1d}.\text{breaks}(i)\right)^2 \\ \quad + \psi_{1d}.\text{coefs}(i,3)\left(t - \psi_{1d}.\text{breaks}(i)\right) + \psi_{1d}.\text{coefs}(i,4) \end{cases} \tag{18}$$

By the determined time set, the mathematical models of x_{1d} (desired position in the surge direction), ψ_{1d} (desired heading angle), y_{1d} (desired position in the sway direction) and z_{1d} (desired position in the heave direction) in relation to time t are then established as shown in Figure 7 based on cubic spline interpolation. For efficient modeling, the desired trajectory model is established empirically with 215 nodes.

The curves of the constructed models of expected longitudinal displacement, heading angle, lateral displacement and vertical displacement in relation to time are continuous and smooth, which meet the requirements of the expected trajectory model. Based on the above analysis, the three-dimensional trajectory model in the constructed hydrothermal area as shown in Figure 8 can be obtained by using Equation (18).

As can be seen from Figure 6, the space desired trajectory curve constructed based on the 215 nodes is continuous and smooth. However, an increasing number of nodes will result in a sharp expansion of the interpolation data set and slower calculation efficiency, which makes it difficult to meet engineering requirements. Moreover, a greater number of piece-wise functions will lead to shorter piece-wise intervals and the positions where the control input changes are more likely to witness abrupt values.

For this reason, it is necessary to optimize the number of nodes used in the desired trajectory model and construct the desired trajectory model in a shorter time. The Levy flight technology is introduced to the slime mold algorithm to optimize the number of nodes and generate a trajectory model meeting the optimization objectives in a shorter time.

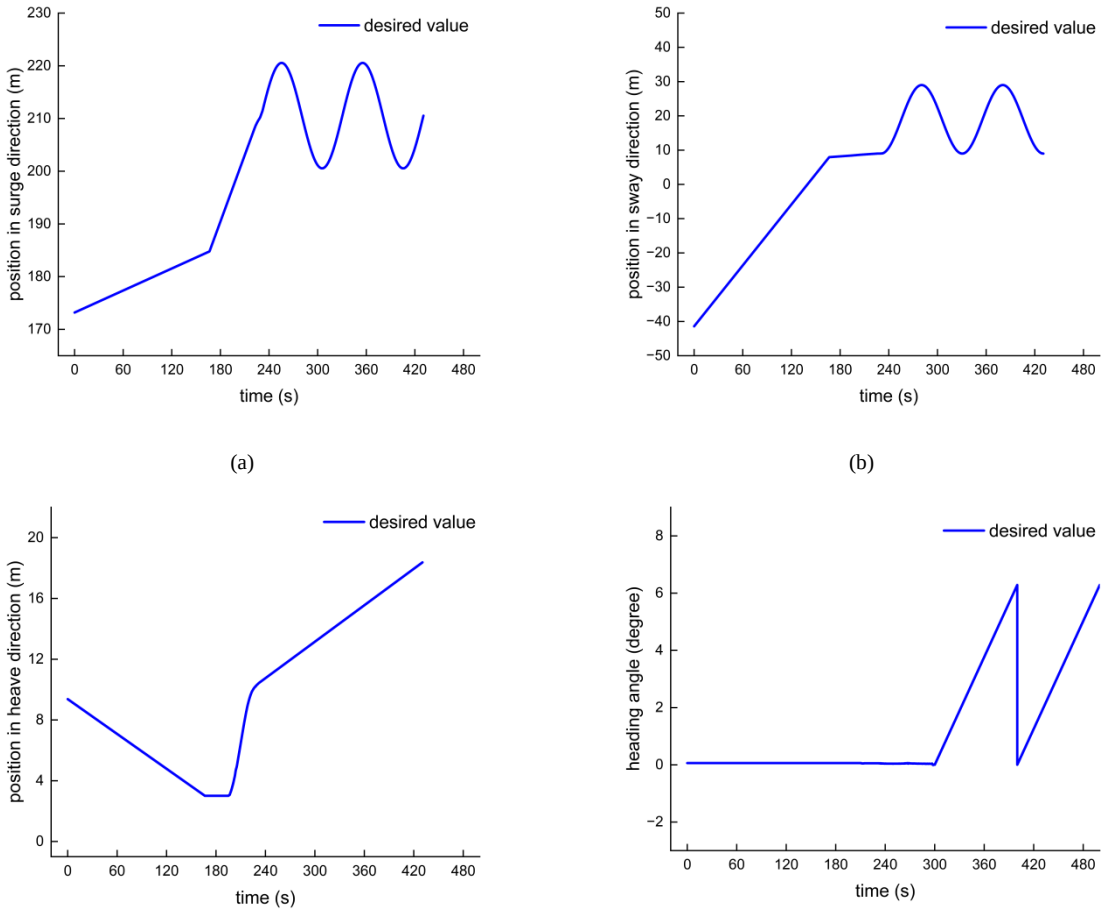

Fig.7 Desired AUV trajectory data. (a) desired position in the surge direction; (b) desired position in the sway direction; (c) desired position in the heave direction; (d) desired heading angle

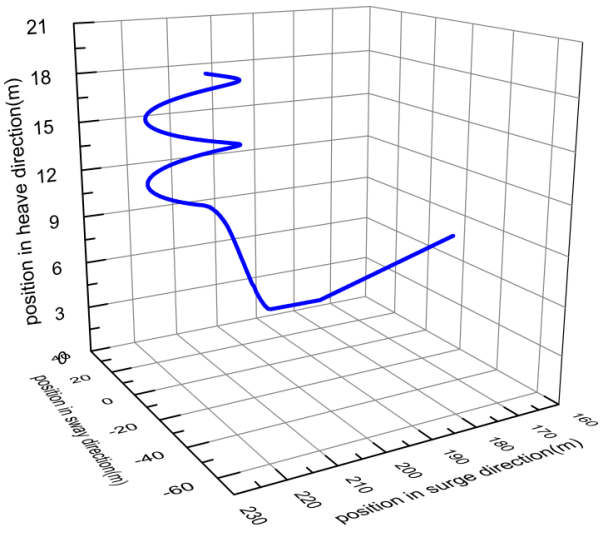

Fig.8 Desired AUV trajectory in space

4.2 Slime mold algorithm

The Slime Mold Algorithm was proposed in 2020 based on the foraging behavior and morphological changes of slime molds [52]. As shown in Table 1, n_o stands for the number of slime molds, $K_i = (K_1, K_2, \ldots K_{dim})$ for the state vector of each individual slime mold, $Weight$ for weight, S_i for fitness, K_{best}^{it} for the position with the highest food concentration in the it-th iteration, p for the factor influencing slime mold state update and vb for the step length when slime molds approach the food. The behaviors include preying, besieging and random moves [53].

Table 1 Variables in slime mold algorithm

Variable	Meaning	Behavior	Meaning
n_o	number of slime molds	*Prey*()	preying
K_i	state vector of each individual	*Besiege*()	besieging
Weight	weight		
$S(i)$	fitness of each individual		
K_{best}^{it}	position with the highest food concentration in the *it*-th iteration		
p	factor influencing slime mold state update		
vb	step length slime molds approaching food		

The space where the slime molds reside is the solution space of the problem to be optimized. The food concentration corresponding to its present position is a potential solution. Each slime mold individual updates its position based on the food concentration and behavior in the present iteration. *Weight*, vb and vc simulate the width changes of the slime mold's vein. As shown in Figure 9, *Weight* is the extent that each slime mold individual determines its next move according to the food information searched by other slime molds. vb means the change of the slime mold's vein diameter. vc means the change of the amount of historical information retained.

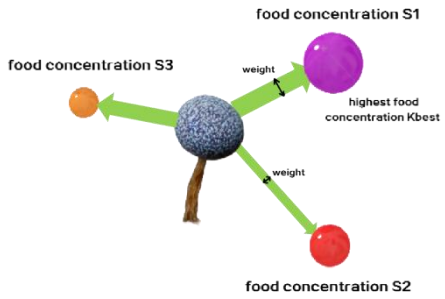

Fig.9 Evaluation of fitness by slime mold individuals

Taking the minimum problem as an example, the behaviors of slime molds are explained as follows:

a) Preying behavior

The slime molds prey according to their present state and the food concentration at their present position. Their next state is determined by r_k and p.

If $r_k < p$, the slime mold will search near the individual with the highest food concentration in the present iteration. Its next state is expressed as follows:

$$K_i^{it+1} = K_{best}^{it} + vb \cdot \left(Weight_i^{it} \cdot K_{r_A}^{it} - K_{r_B}^{it} \right) \tag{19}$$

where it is the number of iterations. K_i^{it} is the position of the i-th individual in the it-th iteration, $i = 1,2,\ldots,n_o$. $vb \in [-a,a]$. $Weight_i^{it}$ is the weight of the i-th individual. $K_{r_A}^{it}$ and $K_{r_B}^{it}$ are random individuals in the it th iteration. $r_k \in [0,1]$ is random.

p determines the update of slime molds:

$$p = \tanh\left| S(i) - DF \right| \tag{20}$$

where $S(i)$ is the fitness of the i-th individual and DF is the optimal fitness value in all iterations.

The range of vb is determined by a that is expressed as follows:

$$a = arc\tanh\left(-\left(\frac{it}{Max\_it} \right) + 1 \right) \tag{21}$$

where Max_it means the maximum number of iterations.

$Weight_i^{it}$ is expressed as follows:

$$Weight_i^{it} = \begin{cases} 1 + r_C \cdot \log_{10}\left(1 + \dfrac{bFit\text{-}S(i)}{bFit - wFit} \right), & condition \\ 1 - r_C \cdot \log_{10}\left(1 + \dfrac{bFit\text{-}S(i)}{bFit - wFit} \right), & others \end{cases} \tag{22}$$

where $r_C \in [0,1]$ is random. $bFit$ and $wFit$ are respectively the best and the worst fitness values in the present iteration. A greater weight means a greater fitness value. $condition$ is the slime mold individuals whose fitness ranks in the top 50%.

If $r_k \geq p$, the slime mold will search according to its present position. Its next state is expressed as follows:

$$K_i^{it+1} = vc * K_i^{it} \tag{23}$$

where $vc \in [-b,b]$ is uniformly distributed and random. b is expressed as follows:

$$b = 1 - \frac{it}{Max\_it} \tag{24}$$

b) Besieging behavior

The besieging behavior simulates the constriction of slime mold's veins. The veins produce propagation waves of different intensity corresponding to the food concentration they detect. Higher food concentration means greater weight in the present area. With low food concentration ($r_D < z$), the slime mold will search randomly. Its next state is expressed as follows:

$$K_i^{it+1} = r_F \cdot (ub - lb) + lb, \; r_D < z \tag{25}$$

where r_D and $r_F \in [0,1]$ are random. z evaluates the random search and the preferential search. ub and lb are respectively the upper and lower bounds of the search space.

Otherwise, the slime mold individual takes the preying move:

$$K_i^{it+1} = \begin{cases} K_{best}^{it} + vb \cdot \left(Weight_i^{it} \cdot K_{r1}^{it} - K_{r2}^{it} \right), \ r_D \geq z, r_k < p \\ vc \cdot K_i^{it}, \ r_D \geq z, r_k \geq p \end{cases} \tag{26}$$

According to Equations (25) and (26), the slime molds can search in all possible directions, which ensures the global optimal solution. According to Equation (26), the slime molds can search in any direction around the optimal solution.

4.3 Improved slime mold algorithm

With high search accuracy, the slime mold algorithm is independent of a strict model, but the relatively slow convergence and the likelihood of local extreme values are the defects. Therefore, improvements are made with the Levy flight technology [54] and the compactness technique [55] to increase the search speed and promote global optimization.

The position changes are expressed as follows based on the Levy flight technology:

$$x_i^{t+1} = x_i^t + \alpha \otimes Levy(\beta) \tag{27}$$

where α is the parameter of step change. $\otimes$ means point-to-point calculation and $Levy(\beta)$ is the flight route [54]. The compactness technique is built on the probabilistic model [55] that represents the original population and completes population evolution.

The perturbation vector (PV) $PV^t = \left[\mu^t, \delta^t \right]$ describes the macroscopic probability distribution of the entire population. μ and δ are respectively the mean value and standard deviation of the perturbation vector. t is the present number of iterations. The probability density function (PDF, $PDF \in [-1,1]$) corresponds to each pair of the mean value and standard deviation. The PDFs generate the solution x_i. The PDF can be converted to the cumulative distribution function (CDF, $CDF \in [0,1]$) that is expressed as follows:

$$CDF = \int_{-1}^{x} PDF dx = \int_{-1}^{x} \sqrt{\frac{2}{\pi}} e^{\frac{(x-\mu)^2}{2\delta^2}} \Bigg/ \delta \left(erf\left(\frac{\mu+1}{\sqrt{2}\delta} \right) - erf\left(\frac{\mu-1}{\sqrt{2}\delta} \right) \right) dx \tag{28}$$

where $x \in [-1,1]$. $erf()$ is the deviation function. The CDF can be further expressed as follows:

$$CDF = \left[erf\left(\frac{\mu+1}{\sqrt{2}\delta} \right) + erf\left(\frac{x-\mu}{\sqrt{2}\delta} \right) \right] \Bigg/ \left[erf\left(\frac{\mu+1}{\sqrt{2}\delta} \right) - erf\left(\frac{\mu-1}{\sqrt{2}\delta} \right) \right] \tag{29}$$

With the PV, x_i can be randomly obtained by the inverse operation of the CDF. As the algorithm proceeds, the PV keeps updating. With two solutions generated, they are compared with the fitness value. The winner and loser are then used to update the PV's standard deviation and mean value:

$$\mu_i^{t+1} = \mu_i^t + \frac{1}{N_p} \left(winner_i - loser_i \right) \tag{30}$$

where N_p is the constant describing the virtual population. δ is updated as follows:

$$\left(\delta_i^{t+1}\right)^2 = \left(\delta_i^t\right)^2 + \left(\mu_i^t\right)^2 - \left(\mu_i^{t+1}\right)^2 + \frac{1}{N_p}\left(winner_i - loser_i\right) \tag{31}$$

The probabilistic model is introduced to replace the slime mold population and the Levy flight technology is adopted to replace the random move so that the slime molds can achieve efficient and expansive search. With the introduction of the probability model, the weight update expression in Equation (22) is updated as follows:

$$Weight^{it} = \begin{cases} 1 + r_C \cdot \log_{10}\left(1 + \dfrac{DF\text{-}S}{DF - wFit}\right), & condition\_cSMA \\ 1 - r_C \cdot \log_{10}\left(1 + \dfrac{DF\text{-}S}{DF - wFit}\right), & others \end{cases} \tag{32}$$

where $condition\_cSMA$ is the constraint of the set random parameters ranging between 0 and 1.

The optimization is organized as follows. When the iteration starts, the position of the slime molds is updated based on the inversely operated and inversely normalized CDFs. As the optimal food concentration updates, the slime molds calculate the weight vector according to the concentration deviation. The next move is determined according to the pre-set parameter that evaluates between random search and preferential search.

With the Levy flight technology, the slime molds make alternately long-and-short moves in accordance with the appropriate step extension factor α. The position changes in a wide range with a small probability will facilitate fast global search.

When the slime molds make the besieging act, the decision of position update is made according to the value of p. Based on the compactness technique, the efficiency of the besieging behavior is intensified and the population parameters are removed. With a position of higher food concentration found, the slime mold individual will search around the said position.

The solutions already generated are compared in view of food concentration to find the highest concentration (*winner*) and the lowest concentration (*loser*). Then the PV is updated.

The improved algorithm based on the probabilistic model enables the slime molds to search rapidly within a wider range, which effectively improves the search speed and local search ability and lays the foundation for the optimization of the number and the sequence of interpolation points in AUV trajectory modeling.

In line with the optimization objectives of the AUV trajectory model, the algorithm flow is composed of the inner cycle and outer cycle as shown in Figure 10. The outer cycle determines the number of interpolation points required for modeling, while the inner cycle constructs the sequence of interpolation points based on the fitness value and the number of interpolation points determined by the outer cycle.

To evaluate the optimization effect, an index function is needed to describe the number and sequence of the interpolation points determined by the trajectory model. With the interpolation point sequence from the inner loop, the index function calculates the cumulative deviations between the trajectory model and all the interpolation points. The index function is defined as follows taking the number of interpolation points and the penalty factor into consideration:

$$\min \Phi_g = \sum_{m=1}^{all} error\_point(i) + a_k \cdot K_k \tag{33}$$

where K_k is the solution from the outer loop. $error\_point$ is the deviation between the i-th interpolation point and the model constructed.

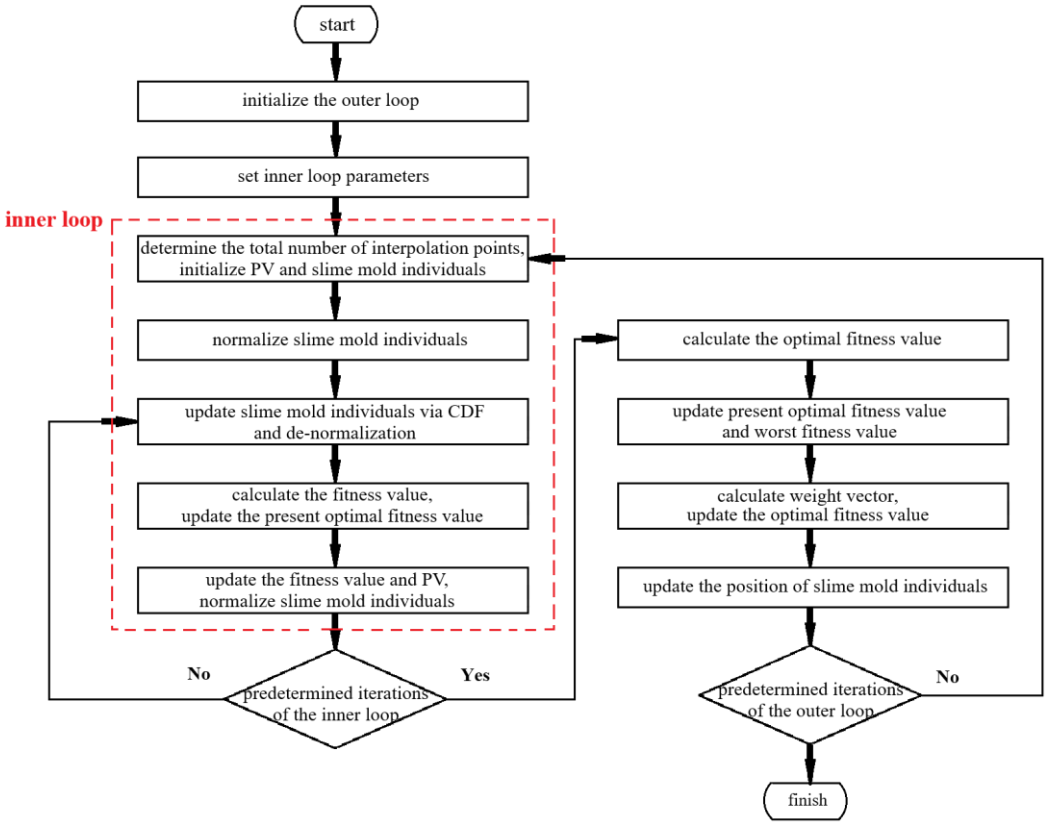

Fig.10 Optimization flow of improved slime mold algorithm

5. Simulation experiments and analysis

On the platform Matlab, the simulation experiments on AUV trajectory modeling and optimization based on the improved slime mold algorithm were carried out corresponding to the 215 path points along the target hydrothermal area. N_p and δ were selected to find how the associated parameters influence the performance of the improved algorithm.

In the simulation experiments, the parameters of the improved slime mold algorithm were defined as follows. In the outer cycle, the slime mold population was defined as $n_o = 10$, the maximum number of iterations as $Max\_iter_1 = 20$, the total number of interpolation points as $all = 215$, the minimum number of interpolation points as $lb_1 = 55$, the evaluation parameter as $z_1 = 0.04$, the step change parameter as $\alpha_1 = 1.1$ and the penalty factor as $\alpha_k = 0.0005$. In the inner cycle, the maximum number of iterations was defined as $Max\_iter_2 = 500$, the lowest interpolation sequence number as $lb_2 = 1$, the evaluation parameter as $z_2 = 0.02$, the step change parameter as $\alpha_2 = 1.0$ and the weight evaluation parameter as $wig = 0.5$. $N_p = [120, 160, 200, 240]$ and $PV = [20, 25, 30, 35]$ were selected for the simulation experiments. All the other parameters were kept consistent throughout the simulation experiments. The simulation results were averaged over 10 runs.

Figure 11 shows the optimization results based on the improved slime mold algorithm under different N_p values. It can be seen that the index function began to converge after approximately 3 iterations. In general, larger N_ps showed quicker convergence and smaller solutions. The minimum optimal solution was found under $N_p = 200$. The number of interpolation points corresponding to the above optimizations were 136, 132, 120 and 128 respectively.

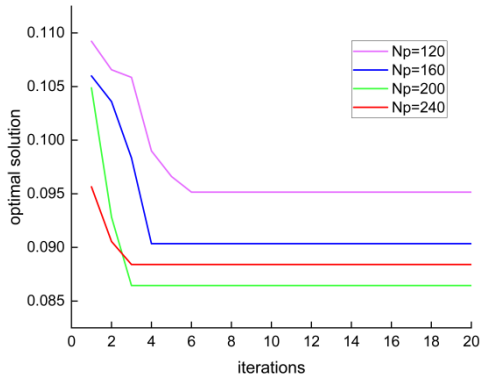

Fig.11 Optimization results of AUV desired trajectory modeling under different N_p values

Figure 12 shows the optimization results under different δ. It can be seen that the index function began to converge after approximately 3 iterations. Larger δ s ($\delta < 30$) showed quicker convergence and smaller solutions. The minimum optimal solution was found with $\delta = 30$. The number of interpolation points corresponding to the above optimizations were 135, 128, 120 and 125 respectively.

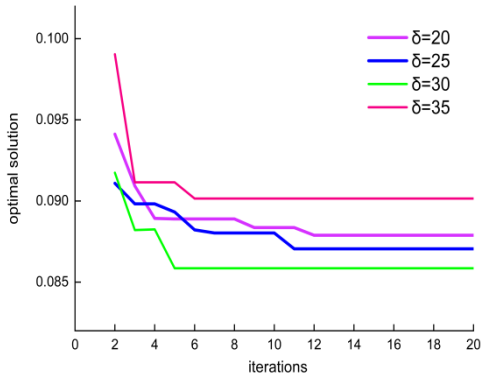

Fig.12 Optimization results of AUV desired trajectory modeling under different δ values

Based on the simulation results, N_p and δ influenced the searchability and efficiency of the improved algorithm. With N_p of approximately 200 and δ of approximately 30 the improved algorithm provided the optimal convergence and the number of interpolation points.

Contrastive experiments were also carried out with parallel optimization algorithms including the slime mold algorithm (SMA), artificial fish swarm algorithm (AFSA), particle swarm optimization (PSO) and compact cuckoo search (CCS).

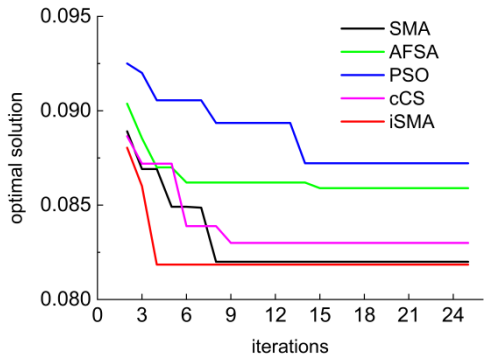

Fig.13 Optimization results of parallel optimization algorithms

As the results shown in Figure 13, all the methods began to converge at approximately the 8th iteration. As shown in Table 2, the PSO method showed the longest searching time and the biggest optimal solution of 0.0872. The AFSA was stuck with a local extremum value for 9 times of iteration before reaching its optimal solution. In contrast, the CCS and the SMA reached their optimal solutions within a shorter time, but the iSMA distinguished itself with the minimum optimal solution within the shortest search time. According to the results, the proposed improved slime mold algorithm showed superior performance with shorter running time by 14.3%, 26.1%, 24.4% and 7.96% and smaller optimal solution value by 0.2%, 4.8%, 6.2% and 1.4% to SMA, AFSA, PSO and CCS respectively.

Table 2 Results of contrastive simulation experiments

Item	SMA	AFSA	PSO	CCS	iSMA
Number of interpolation points	120	125	117	117	114
Optimal solution	0.0820	0.0859	0.0872	0.0830	0.0818
Running time	426.38 s	494.55 s	483.36 s	396.82 s	365.20 s

6. Pool test and analysis

The trajectory tracking control test of varying heading angle, varying velocity in surge direction and varying depth, was conducted based on the control system of the platform. According to the desired trajectory tracking model in Figure 14, the AUV was released and dived along the slope. Then it was expected to complete the depth control as if passing the area of dense hydrothermal bodies before going up and circling above the hydrothermal vent in a rising spiral. The test lasted 350 control beats, each beat of 0.5s. The environment of the benthonic hydrothermal zone was simulated in the test, including the influence of water current and hydrothermal eruption. The current flowed at 0.15m/s with direction of 60°in the horizontal plane and the hydrothermal flowed at 0.18m/s (where the AUV executed the detection task) with direction of 2.5° in the vertical plane.

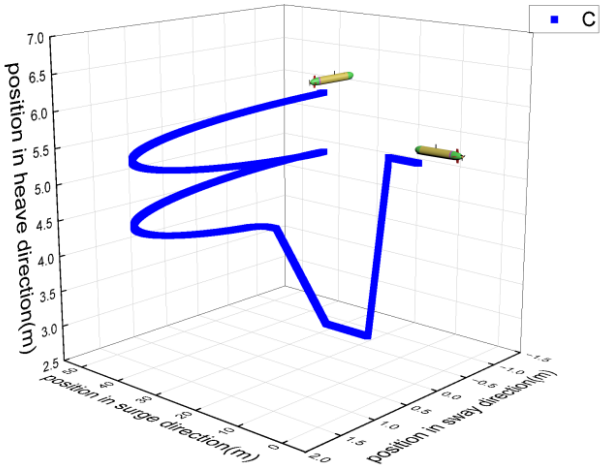

Fig.14 Desired trajectory model

6.1 Tracking control of heading angle

In the heading angle tracking control, the initial heading angle of the AUV was -58°and the desired heading angle at the end of tracking was 150°. Changes of the heading angle were designed during the ascending spiral detection in order to test the optimization method propped. The desired heading angle tracking model optimized based on the proposed improved slime mold algorithm was constructed as follows:

$$
\begin{aligned}
&\psi_{n\_1d} = \text{spline}\left(Yaw_{n\_1}, T_{n\_1}, t_1\right) \\
&\psi_{n\_1d}(i_{n\_1},1) = \psi_{n\_1d}.\text{coefs}\left(i_{n\_1},1\right)\left(t-\psi_{n\_1d}.\text{breaks}\left(i_{n\_1}\right)\right)^3 \\
&\quad + \psi_{n\_1d}.\text{coefs}\left(i_{n\_1},2\right)\left(t-\psi_{n\_1d}.\text{breaks}\left(i_{n\_1}\right)\right)^2 \\
&\quad + \psi_{n\_1d}.\text{coefs}\left(i_{n\_1},3\right)\left(t-\psi_{n\_1d}.\text{breaks}\left(i_{n\_1}\right)\right) \\
&\quad + \psi_{n\_1d}.\text{coefs}\left(i_{n\_1},4\right) \qquad if\ T_{i_{n\_1}} \le t \le T_{i_{n\_1}+1}
\end{aligned} \tag{34}
$$

where n_1 was the number of interpolation points in the optimized desired heading angle model. ψ_{n_1d} was made up of (n_1-1) cubic functions. $Yaw_{n\_1} = \left[Yaw_1 \ldots Yaw_{n\_1}\right] \in R^{1\times n-1}$ and $T_{n\_1} = \left[T_1 \ldots T_{n\_1}\right] \in R^{1\times n-1}$ were time intervals, $i_{n\_1} = 1,2,\ldots,n\_1$. $\psi_{n\_1d}.\text{coefs}$ were the function coefficients obtained by spline interpolation and $\psi_{n\_1d}.\text{breaks}$ were the breakpoints.

The number of interpolation points in the heading angle tracking control model was 208 with the interpolation error of 0.33. As can be seen from Figure 15(a), the actual trajectory curve of the AUV was highly coincident with the desired heading angle curve, with barely any fluctuations except for the distinct difference between the desired and actual heading angles at the beginning. Furthermore, as shown in Figure 15(b), the control deviations ranged between -3°and 2°during the ascending spiral detection, with the arithmetic mean value of -0.361°and the standard deviation of 0.158°.

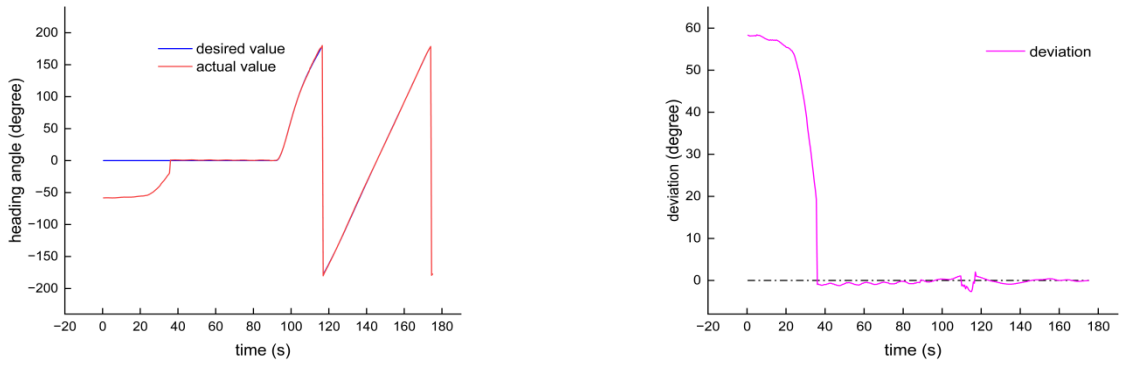

(a) (b)

Fig.15 Results of heading angle tracking control. (a) desired heading angle and actual heading angle; (b) deviation of heading angle tracking

6.2 Tracking control of velocity in surge direction

In the velocity tracking control, the initial velocity of the AUV was 0m/s and the desired velocity at the end of tracking was 0.38m/s. Different velocities were designed in different sections along the tracking route. The desired velocity tracking model optimized based on the proposed improved slime mold algorithm was constructed as follows:

$$
\begin{aligned}
u_{n\_2d} &= \text{spline}\left(U_{n\_2}, T_{n\_2}, t_1\right) \\
u_{n\_2d}(i_{n\_2},1) &= u_{n\_2d}.\text{coefs}\left(i_{n\_2},1\right)\left(t - u_{n\_2d}.\text{breaks}\left(i_{n\_2}\right)\right)^3 \\
&+ u_{n\_2d}.\text{coefs}\left(i_{n\_2},2\right)\left(t - u_{n\_2d}.\text{breaks}\left(i_{n\_2}\right)\right)^2 \\
&+ u_{n\_2d}.\text{coefs}\left(i_{n\_2},3\right)\left(t - u_{n\_2d}.\text{breaks}\left(i_{n\_2}\right)\right) \\
&+ u_{n\_2d}.\text{coefs}\left(i_{n\_2},4\right) \qquad if\ T_{i_{n\_2}} \le t \le T_{i_{n\_2}+1}
\end{aligned} \tag{35}
$$

where n_2 was the number of interpolation points in the optimized desired velocity model. u_{n_2d} was made up of (n_2-1) cubic functions. $U_{n\_2} = \left[U_1 \ldots U_{n\_2}\right] \in R^{1\times n\_2}$ and $T_{n\_2} = \left[T_1 \ldots T_{n\_2}\right] \in R^{1\times n\_2}$ were time intervals. $u_{n\_2d}.\text{coefs}$ were the function coefficients obtained by spline interpolation. $u_{n\_2d}.\text{breaks}$ were the break points.

The number of interpolation points in the velocity tracking model was 208 with the interpolation error of 0.26. As can be seen from Figure 16(a), the actual trajectory curve of the AUV was highly coincident with the desired velocity curve except for the minor overshoots. In sections of successive velocity changes, the actual velocity well tracked the desired values. As shown in Figure 16(b), the overall deviations ranged between -0.1m/s and 0.1m/s. The maximum deviation was no more than 0.1m/s, with the arithmetic mean value of -0.005m/s and the standard deviation of 0.023m/s. The velocity tracking results were responsive during the control.

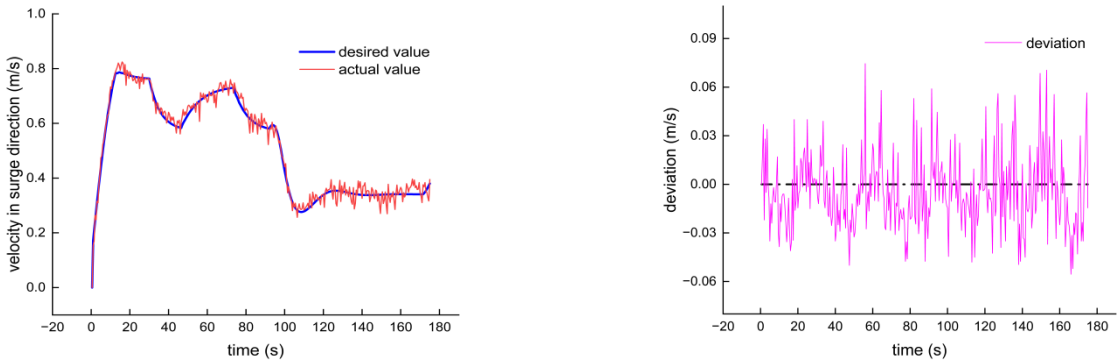

(a) (b)

Fig.16 Results of velocity tracking control. (a) desired velocity and actual velocity; (b) deviation of velocity tracking

6.3 Tracking control of depth

In the depth tracking control, the AUV was released at 4.3m and the desired height at the end of tracking was 3.5m. In order to verify the tracking performance based on the proposed improved modeling method, varying heights were designed at the slope, the dense hydrothermal bodies and the hydrothermal vent. The desired depth tracking model optimized based on the proposed improved slime mold algorithm was constructed as follows:

$$
\begin{aligned}
& z_{n\_3d} = \text{spline}\left(Z_{n\_3}, T_{n\_3}, t_1\right) \\
& z_{n\_3d}(i_{n\_3},1) = z_{n\_3d}.\text{coefs}\left(i_{n\_3},1\right)\left(t - z_{n\_3d}.\text{breaks}\left(i_{n\_3}\right)\right)^3 \\
& \quad + z_{n\_3d}.\text{coefs}\left(i_{n\_3},2\right)\left(t - z_{n\_3d}.\text{breaks}\left(i_{n\_3}\right)\right)^2 \\
& \quad + z_{n\_3d}.\text{coefs}\left(i_{n\_3},3\right)\left(t - z_{n\_3d}.\text{breaks}\left(i_{n\_3}\right)\right) \\
& \quad + z_{n\_3d}.\text{coefs}\left(i_{n\_3},4\right) \qquad if\ T_{i_{n\_3}} \le t \le T_{i_{n\_3}+1}
\end{aligned} \tag{36}
$$

where n_3 was the number of interpolation points in the optimized desired depth tracking model. z_{n_3d} was made up of (n_3-1) cubic functions. $Z_{n\_3} = \left[Z_1 \ldots Z_{n\_3}\right] \in R^{1\times n\_3}$ and $T_{n\_3} = \left[T_1 \ldots T_{n\_3}\right] \in R^{1\times n\_3}$ were time intervals. $z_{n\_3d}.\text{coefs}$ were the function coefficients obtained by spline interpolation and $z_{n\_3d}.\text{breaks}$ were the breakpoints.

The number of interpolation points in the depth tracking model was 208 with the interpolation error of 0.22. As can be seen from Figure 17(a), the actual trajectory curve was smooth and stable except for the insignificant deviation when the AUV was released. As shown in Figure 17(b), the tracking deviation gradually converged and fluctuated between -0.3m and 0.25m, with the maximum deviation of no more than 0.3m, the arithmetic mean value of -0.006m and the standard deviation of 0.101m. The depth tracking showed a desirable effect.

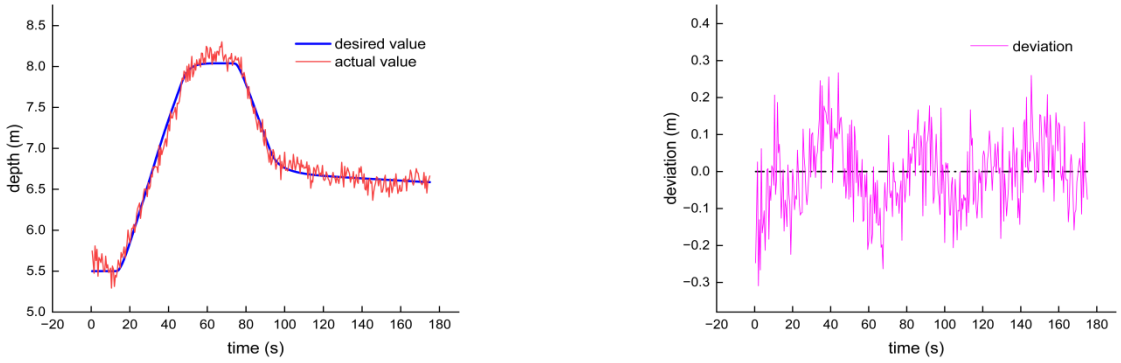

(a) (b)

Fig.17 Results of depth tracking control. (a) desired depth and actual depth; (b) deviation of depth tracking

Table 3 Analysis of tracking control results after the 80th control beat

	initial value	**maximum deviation**	**arithmetic mean of deviation**	**standard deviation**
tracking of heading angle	-58°	-2.652°	-0.171°	0.652°
tracking of velocity in surge direction	0 m/s	0.071 m/s	-0.003 m/s	0.025 m/s
tracking of depth	5.7 m	0.267 m	-0.004 m	0.095 m

In the pool test that fully considered the complex and challenging benthonic hydrothermal environment (including the slopes, dense areas of hydrothermal deposits, hydrothermal vents, ocean currents and hydrothermal flows, etc.), the trajectory tracking performance based on the improved slime mold modeling method was desirable and well able to meet the accuracy requirements in engineering application. The

maximum deviation, the arithmetic mean value of the deviation and the standard deviation after the 80th control beat in the tracking control are provided in Table 3.

7. Conclusion

In this study, an improved slime mold algorithm was developed for the optimization of desired trajectory modeling for detection and control operations in benthonic hydrothermal areas. In traditional AUV trajectory modeling, the trajectory model was typically constructed with the time points simply inserted into the path, which made it difficult to produce a specific and smooth trajectory. The classical spline interpolation method is capable of producing smooth curves, but a large number of nodes are required in the face of complex routes. To achieve efficient and accurate desired trajectory modeling for AUV operations in benthonic hydrothermal areas, the cubic spline interpolation was adopted for predetermined AUV waypoints processing. An improved slime mold algorithm was proposed to optimize the interpolation points in the trajectory modeling. In addition, the Levy flight technology and compactness technique were introduced to improve the global search ability, increase the search speed and accuracy of the proposed optimization algorithm.

The study on the influencing factors, namely the virtual population and the PV's standard deviation, was conducted to provide the recommended parameters leading to short convergence time and high search accuracy. In the contrastive simulation experiments with peer optimization methods, the proposed improved slime mold algorithm showed the abilities to effectively avoid local extremum and provide a high-precision desired trajectory model within a shorter search time. Moreover, the pool test was also carried out in trajectory tracking control of heading angle, velocity in surge direction and depth. After the 80th control beat during the tracking control, the maximum instantaneous tracking deviation of the heading angle was no more than 2.5° with the steady-state tracking deviation within 0.1° when the heading angle changed over 260°. The tracking of velocity in the surge direction was stable on the whole, with the arithmetic mean value of deviation -0.003m/s, the maximum overshoot of 0.071 m/s and the standard deviation of 0.025 m/s. The same stable results can be also seen in the depth tracking with the arithmetic mean value of deviation -0.004m, the maximum overshoot of 0.267 m and the standard deviation of 0.095 m. The pool test verified the effectiveness and feasibility of the proposed optimization method in tracking model construction for benthonic hydrothermal area operations.

In accordance with the constructive simulation experiments with the AFSA, PSO, and CCS, the improved SMA can satisfy the requirement for accurate modeling of benthonic hydrothermal trajectory, with a fewer number of nodes, shorter search progress and improved search accuracy. Its advantages are desired in engineering practice in the work context of challenging conditions including varying currents and disturbance. The present study is limited with analysis of the impacts of ambient noise and uncertainty in sensor data upon the proposed improved SMA. In addition, the interference of external changes and unpredictable factors on AUV trajectory control is also open to further discussion.

The test platform in this study is propeller-rudder driven, but theoretically, the research findings apply to the AUVs with no rudder or wing. Further studies are planned to be carried out on AUVs of different dimensions and propulsion systems. As the present test platform is under-actuated, the control characteristics and fault tolerance in the case of actuator failure are also the directions in future research to improve the usability and applicability of the present test platform.

ACKNOWLEDGMENT

This research was supported by National Natural Science Foundation of China (grant number 51779058, 51709061, 52071099). We express gratitude to Yushan Sun, Guocheng Zhang, Zhuo Wang for the support of National Natural Science Foundation of China, and especially Yushan Sun for encouragement and help.

REFERENCES

[1] Bisson, K., McMonagle, H., Iglesias, I., Halfter, S., Gallo, N., 2023. Five reasons to take the precautionary approach to deep sea exploitation. *Communications Earth & Environment*, 4(1), 152. https://doi.org/10.1038/s43247-023-00823-4

[2] Sharma, H., Sharma, G., Kumar, N., 2024. AI-assisted secure data transmission techniques for next-generation HetNets: A review. *Computer Communications*, 215, 74–90. https://doi.org/10.1016/j.comcom.2023.12.015

[3] Deepa, M., Bikramjit, B., 2024. Biomechanical analysis of peri-prosthetic bone response to hybrid threaded zirconia dental implants: An in silico model. *Journal of the Mechanical Behavior of Biomedical Materials*, 150, 106310. https://doi.org/10.1016/j.jmbbm.2023.106310

[4] Ashit, H., Walid, T., Gao, X.H, 2024. Developing a Machine-Learning Model to Predict Clash Resolution Options. *Journal of Computing in Civil Engineering*, 38(2), 5548. https://doi.org/10.1061/JCCEE5.CPENG-5548

[5] Ugur, K., Francisco, V., Murat, A., Selcuk, E., Luis, A., Hikmet, K.T., 2024. Deep learning-based forecasting modeling of micro gas turbine performance projection: An experimental approach. *Engineering Applications of Artificial Intelligence*, 130, 107769. https://doi.org/10.1016/j.engappai.2023.107769

[6] Shi, H., Zheng, R., Zhang, Q., Yuan, J., Wang, R., Cheng, M., Zou, Y., 2023. Numerical investigation of multi-nozzle ejector device with inclined nozzles for marine gas turbine. *Brodogradnja*, 74(4), 1–16. https://doi.org/10.21278/brod74401

[7] Shankar, D. D., Azhakath, A. S., Khalil, N., Sajeev, J., Mahalakshmi, T., Sheeba, K., 2024. Data mining for cyber biosecurity risk management – A comprehensive review. *Computers & Security*, 137, 103627. https://doi.org/10.1016/j.cose.2023.103627

[8] Marlin, S., Sundarsingh, J., 2024. A comprehensive comparative study on intelligence based optimization algorithms used for maximum power tracking in grid-PV systems. *Sustainable Computing-Informatics & Systems*, 41, 100946. https://doi.org/10.1016/j.suscom.2023.100946

[9] Wang, Z., Wei, Z., Yu, C., Cao, J., Yao, B., Lian, L., 2023. Dynamic modeling and optimal control of a positive buoyancy diving autonomous vehicle. *Brodogradnja*, 74(1), 19–40. https://doi.org/10.21278/brod74102

[10] Sahin, O. S., Kahramanoglu, E., Cakici, F., Pesman, E., 2023. Control of dynamic trim for planing vessels with interceptors in terms of comfort and minimum drag. *Brodogradnja*, 74(1), 1–17. https://doi.org/10.21278/brod74101

[11] Guerra, A., Azevedo, A., Amorim, F., Soares, J., Neuparth, T., Santos, M. M., Martins, I., Colaço, A., 2024. Using a food web model to predict the effects of Hazardous and Noxious Substances (HNS) accidental spills on deep-sea hydrothermal vents from the Mid-Atlantic Ridge (MAR) region. *Marine pollution bulletin*, 199, 115974. https://doi.org/10.1016/j.marpolbul.2023.115974

[12] Pokhile, N. P., Afanasiev, V. P., Tolstov, A. V., Kruk, N. N., Pokhilenko, L. N., Ivanova, O. A, 2023. Perspectives of the Development and Problems of Exploration of a Resource Base of Deficient Strategic Mineral Deposits of Siberia. *Geology of Ore Deposits*, 65(5), 494–509. https://doi.org/10.1134/S1075701523050082

[13] Yoon, H. C., Kim, J. H, 2024. The impacts of scaled capillary pressure combined with coupled flow and geomechanics on gas hydrate deposits. *Geomechanics for Energy and the Environment*, 37, 100529. https://doi.org/10.1016/j.gete.2023.100529

[14] Ibrahim, O., 2023. Predicting main engine power and emissions for container, cargo, and tanker ships with artificial neural network analysis. *Brodogradnja*, 74(2), 77–94. https://doi.org/10.21278/brod74204

[15] Yu, Z., Jin, Z. Y., Wang, K. C., Zhang, C. Y., Chen, J. W, 2023. Design and Study of Mechanical Cutting Mechanism for Submarine Cable Burial Machine. *Journal of marine science and engineering*, 11(12), 2371. https://doi.org/10.3390/jmse11122371

[16] Fujinami, K., Takuno, R., Sato, I., Shimmura, T., 2023. Evaluating Behavior Recognition Pipeline of Laying Hens Using Wearable Inertial Sensors. *Sensors*, 23, 5077. https://doi.org/10.3390/s23115077

[17] Gou, S. H., Huang, D. P., Liao, S. P., Luo, F., Yuan, Y., Liu, L., Wen, X. M, 2024. Online defect detection method of optical cable pitch based on machine vision technology and deep learning algorithms. *Optics and Laser Technology*, 171, 110344. https://doi.org/10.1016/j.optlastec.2023.110344

[18] Khaled, A., 2023. Modeling of PID controlled 3DOF robotic manipulator using Lyapunov function for enhancing trajectory tracking and robustness exploiting Golden Jackal algorithm. *ISA transactions*, 145, 190–204. https://doi.org/10.1016/j.isatra.2023.11.033

[19] Wang, Y., Wang, Y. J., Li, Y. X., Ren, C., 2023. Dynamic Modeling and Robust Trajectory Tracking Control of a Hybrid Propulsion-Based Small Underwater Robot. *Journal of Marine Science and Engineering*, 11, 1934. https://doi.org/10.3390/jmse11101934

[20] Aner, E. A., Awad, I., 2023. Modeling and Trajectory Tracking Control for a Multi-Section Continuum Manipulator. *Journal of Intelligent & Robotic Systems*, 108, 49. https://doi.org/10.1007/s10846-023-01896-1

[21] Chen, G. F., Sheng, M. W., Wan, L., Liu, Y. H., Zhang, Z. Y., Xu, Y. F, 2022. Tracking control for small autonomous underwater vehicles in the Trans-Atlantic Geotraverse hydrothermal field based on the modeling trajectory. *Applied Ocean Research*, 127, 103281. https://doi.org/10.1016/j.apor.2022.103281

[22] Wu, G., Li, Y., Jiang, C., Wang, C., Guo, J., Cheng, R., 2022. Multi-vessels collision avoidance strategy for autonomous surface vehicles based on genetic algorithm in congested port environment. *Brodogradnja*, 73(3), 69–91. https://doi.org/10.21278/brod73305

[23] Bao, H., Zhu, H. T, 2022. Modeling and Trajectory Tracking Model Predictive Control Novel Method of AUV Based on CFD Data. *Sensors*, 22, 4234. https://doi.org/10.3390/s22114234

[24] Dong, D., Ye, H. T., Luo, W. G., Wen, J. Y., Huang, D, 2023. Fast Trajectory Tracking Control Algorithm for Autonomous Vehicles Based on the Alternating Direction Multiplier Method (ADMM) to the Receding Optimization of Model Predictive Control (MPC). *Sensors*, 23, 8391. https://doi.org/10.3390/s23208391

[25] Xiao, Z. X., Hu, M. H., Fu, C. Y., Qin, D. T., 2023. Model predictive trajectory tracking control of unmanned vehicles based on radial basis function neural network optimisation. *Proceedings of the Institution of Mechanical Engineers, Part D: Journal of Automobile Engineering*, 237, 347–361. https://doi.org/10.1177/09544070221080158

[26] Qian, Z. L., Lyu, W. C., Dai, Y. Z., Xu, J., 2022. A Consensus-Based Model Predictive Control with Optimized Line-of-Sight Guidance for Formation Trajectory Tracking of Autonomous Underwater Vehicles. *Journal of Intelligent & Robotic Systems*, 106, 15. https://doi.org/10.1007/s10846-022-01710-4

[27] Yu, D. J., Deng, F., Wang, H. Y., Hou, X. H., Yang, H. L., Shan, T. K, 2022. Real-Time Weight Optimization of a Nonlinear Model Predictive Controller Using a Genetic Algorithm for Ship Trajectory Tracking. *Journal of Marine Science and Engineering*, 10, 1110. https://doi.org/10.3390/jmse10081110

[28] Duan, K. R., Fong, S., Chen C. L, 2022. Philip. Reinforcement learning based model-free optimized trajectory tracking strategy design for an AUV. *Neurocomputing*, 469, 289–297. https://doi.org/10.1016/j.neucom.2021.10.056

[29] Wang, H. J., Ren, J. F., Han, M. X., Wang, Z., Zhang, K., Wang, X. N., 2023. Robust adaptive three-dimensional trajectory tracking control for unmanned underwater vehicles with disturbances and uncertain dynamics. *Ocean Engineeering*, 289, 116184. https://doi.org/10.1016/j.oceaneng.2023.116184

[30] Wang, T. M., Wei, Y. H., Peng, X. Y., Huang, L., 2023. Trajectory tracking of autonomous underwater vehicle under disturbance based on time-delay adaptive high-order sliding mode control. *Ocean Engineeering*, 288, 116081. https://doi.org/10.1016/j.oceaneng.2023.116081

[31] Zhu, Z. B., Duan, Z. Q., Qin, H. D., Xue, Y. F, 2023. Adaptive neural network fixed-time sliding mode control for trajectory tracking of underwater vehicle. *Ocean Engineeering*, 287, 115864. https://doi.org/10.1016/j.oceaneng.2023.115864

[32] Hosseini, M., Ranjbar, N. A., Rostami, S. J. S., 2023. Trajectory tracking control of an underwater vehicle in the presence of disturbance, measurement errors, and actuator dynamic and nonlinearity. *Robotica*, 41, 3059–3078. https://doi.org/10.1017/S0263574723000875

[33] Thanh, P. N. N., Thuyen, N. A., Anh, H. P. H., 2023. Adaptive fuzzy 3-D trajectory tracking control for autonomous underwater vehicle (AUV) using modified integral barrier lyapunov function, *Ocean Engineeering*, 283, 115027. https://doi.org/10.1016/j.oceaneng.2023.115027

[34] Przemyslaw, H., 2023. Trajectory Tracking Nonlinear Controller for Underactuated Underwater Vehicles Based on Velocity Transformation. *Journal of Marine Science and Engineering*, 11(3), 509. https://doi.org/10.3390/jmse11030509

[35] Bingul, Z., Gul, K., 2023. Intelligent-PID with PD Feedforward Trajectory Tracking Control of an Autonomous Underwater Vehicle. *Machines*, 11(2), 300. https://doi.org/10.3390/machines11020300

[36] Fatemeh, S., Arefi, M., Abooee, A., 2023. Command filtered-based neuro-adaptive robust finite-time trajectory tracking control of autonomous underwater vehicles under stochastic perturbations. *Neurocomputing*, 519, 158–172. https://doi.org/10.1016/j.neucom.2022.11.005

[37] Jesus, G., Ahmed, C., Jorge, T., Vincent, C., 2023. Time-delay high-order sliding mode control for trajectory tracking of autonomous underwater vehicles under disturbances. *Ocean Engineeering*, 268, 113375. https://doi.org/10.1016/j.oceaneng.2022.113375

[38] Ma, C. P., Tang, Y., Lei, M., Jiang, D. P., Luo, W. Z, 2022. Trajectory tracking control for autonomous underwater vehicle with disturbances and input saturation based on contraction theory. *Ocean Engineeering*, 266, 112731. https://doi.org/10.1016/j.oceaneng.2022.112731

[39] Xue, G., Liu, Y. J., Shi, Z. J., Guo, L., Li, Z. T, 2022. Research on Trajectory Tracking Control of Underwater Vehicle Manipulator System Based on Model-Free Adaptive Control Method. *Journal of Marine Science and Engineering*, 10, 652. https://doi.org/10.3390/jmse10050652

[40] Chen, G. F., Wan, L., Jiang, C. M., Zhang, Y. H., Liu Y. H., Zhang, Z. Y., Xu, Y. F, 2023. Dynamic event-triggered observer-based control for autonomous underwater vehicles in the Trans-Atlantic Geotraverse hydrothermal field using rotation matrices. *Ocean Engineeering*, 281, 114961. https://doi.org/10.1016/j.oceaneng.2023.114961

[41] Jiang, C., Zhang, H., Wan, L., Lv, J., Wang, J., Tang, J., Wu, G., He, B., 2023. Design and Verification of Deep Submergence Rescue Vehicle Motion Control System. *Sensors*, 23, 6772. https://doi.org/10.3390/s23156772

[42] Jiang, C., Lv, J., Wan, L., Wang, J., He, B., Wu, G, 2023. An Improved S-Plane Controller for High-Speed Multi-Purpose AUVs with Situational Static Loads. *Journal of Marine Science and Engineering*, 11, 646. https://doi.org/10.3390/jmse11030646

[43] Byun, S., Papaelias, M., Márquez, F. P. G., Lee, D., 2022. Fault-Tree-Analysis-Based Health Monitoring for Autonomous Underwater Vehicle. *Journal of Marine Science and Engineering*, 10(12), 1855. https://doi.org/10.3390/jmse10121855

[44] Cotroneo, D., Simone, L. D., Natella, R., 2021. Timing Covert Channel Analysis of the VxWorks MILS Embedded Hypervisor under the Common Criteria Security Certification. *Computers & Security*, 106, 102307. https://doi.org/10.1016/j.cose.2021.102307

[45] Kim, H. J., Yoo, S. J, 2024. Adaptive fixed-time containment control of uncertain underactuated underwater vehicles under dynamic event-driven mechanism. *Ocean Engineeering*, 291, 116488. https://doi.org/10.1016/j.oceaneng.2023.116488

[46] Wibisono, A., Piran, M. J., Song, H. K., Lee, B. M, 2023. A Survey on Unmanned Underwater Vehicles: Challenges, Enabling Technologies, and Future Research Directions. *Sensors*, 23, 7321. https://doi.org/10.3390/s23177321

[47] Shakirzyanov, R. M., Shleymovich, M. P., Novikova S. V, 2023. Method for Unmanned Vehicles Automatic Positioning Based on Signal Radially Symmetric Markers Recognition of Underwater Targets. *Automation and Remote Control*, 84(7), 734–752. https://doi.org/10.1134/S000511792307010X

[48] MorerasMarti, A., FoxPowell, M., Zerkle, A. L., Stueeken, E., Gazquez, F., Brand, H. E. A., Galloway, T., Purkamo, L., Cousins, C.R., 2021. Volcanic controls on the microbial habitability of Mars-analogue hydrothermal environments. *Geobiology*, 19(5), 489–509. https://doi.org/10.1111/gbi.12459

[49] Zhou, Y., Liu, H. L., Feng, C. G., Lu, Z. Q., Liu, J., Huang, Y. A., Tang, H. H., Xu, Z. H., Pu, Y. J., Zhang, H. B., 2023. Genetic adaptations of sea anemone to hydrothermal environment. *Science advances*, 9(42), 474. https://doi.org/10.1126/sciadv.adh0474

[50] Hosseini, M., Ranjbar, N. A., Rostami, S. J. S., 2023. Trajectory tracking control of an underwater vehicle in the presence of disturbance, measurement errors, and actuator dynamic and nonlinearity. *Robotica*, 41(10), 3059–3078. https://doi.org/10.1017/S0263574723000875

[51] Tayebi, S., Momani, S., Abu, A. O., 2022. The cubic B-spline interpolation method for numerical point solutions of conformable boundary value problems. *Alexandria Engineering Journal*, 61(2), 1519–1528. https://doi.org/10.1016/j.aej.2021.06.057

[52] Li, S. M., Chen, H. L., Wang, M. J., Ali, A. H., Seyedali, M., 2020. Slime mould algorithm: A new method for stochastic optimization. *Future Generation Computer Systems*, 111, 300–319. https://doi.org/10.1016/j.future.2020.03.055

[53] Chakraborty, P., Nama, S., Saha, A. K., 2022. A hybrid slime mould algorithm for global optimization. *Multimedia Tools and Applications*, 82(15), 22441–22467. https://doi.org/10.1007/s11042-022-14077-3

[54] Joshi, S. K., 2023. Levy flight incorporated hybrid learning model for gravitational search algorithm. *Knowledge-Based Systems*, 265, 110374. https://doi.org/10.1016/j.knosys.2023.110374

[55] Jaiswal, D., Kalita, J. C., 2023. An efficient high-order compact approach for spiral wave dynamics by the FHN model. *Journal of Computational Science*, 73, 102147. https://doi.org/10.1016/j.jocs.2023.102147